

See discussions, stats, and author profiles for this publication at: <https://www.researchgate.net/publication/282346092>

# The Morphology of TiO<sub>2</sub> (B) Nanoparticles

ARTICLE *in* JOURNAL OF THE AMERICAN CHEMICAL SOCIETY · SEPTEMBER 2015

Impact Factor: 12.11 · DOI: 10.1021/jacs.5b08434

---

READS

77

## 4 AUTHORS, INCLUDING:



Xiao Hua

Université de Fribourg

6 PUBLICATIONS 228 CITATIONS

[SEE PROFILE](#)



Clare P Grey

University of Cambridge

431 PUBLICATIONS 11,553 CITATIONS

[SEE PROFILE](#)

# The Morphology of $\text{TiO}_2$ (B) Nanoparticles

Xiao Hua,<sup>†</sup> Zheng Liu,<sup>‡</sup> Peter G. Bruce,<sup>§</sup> and Clare P. Grey\*,<sup>†</sup>

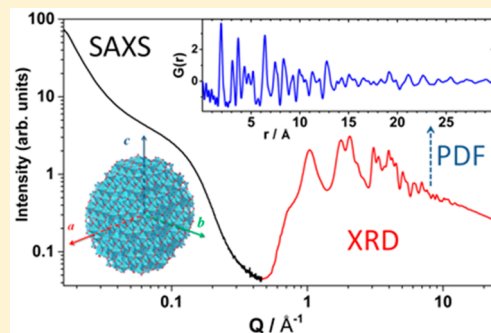
<sup>†</sup>Department of Chemistry, University of Cambridge, Lensfield Road, Cambridge CB2 1EW, United Kingdom

<sup>‡</sup>School of Chemistry, University of St. Andrews, North Haugh, St. Andrews, Fife KY16 9ST, United Kingdom

<sup>§</sup>Department of Materials, University of Oxford, Parks Road, Oxford OX1 3PH, United Kingdom

## Supporting Information

**ABSTRACT:** The morphology of a nanomaterial (geometric shape and dimension) has a significant impact on its physical and chemical properties. It is, therefore, essential to determine the morphology of nanomaterials so as to link shape with performance in specific applications. In practice, structural features with different length scales are encoded in a specific angular range of the X-ray or neutron total scattering pattern of the material. By combining small- and wide-angle scattering (typically X-ray) experiments, the full angular range can be covered, allowing structure to be determined accurately at both the meso- and the nanoscale. In this Article, a comprehensive morphology analysis of lithium-ion battery anode material,  $\text{TiO}_2$  (B) nanoparticles (described in Ren, Y.; Liu, Z.; Pourpoint, F.; Armstrong, A. R.; Grey, C. P.; Bruce, P. G. *Angew. Chem. Int. Ed.* **2012**, *51*, 2164), incorporating structure modeling with small-angle X-ray scattering (SAXS), pair distribution function (PDF), and X-ray powder diffraction (XRD) techniques, is presented. The particles are oblate-shaped, contracted along the [010] direction, this particular morphology providing a plausible rationale for the excellent electrochemical behavior of these  $\text{TiO}_2$ (B) nanoparticles, while also provides a structural foundation to model the strain-driven distortion induced by lithiation. The work demonstrates the importance of analyzing various structure features at multiple length scales to determine the morphologies of nanomaterials.



## INTRODUCTION

In recent years, nanostructured materials with various morphologies including, but not limited to, nanoparticles,<sup>1</sup> nanotubes,<sup>2</sup> nanowires,<sup>3</sup> and more complex micro-/nano-hierarchical structures<sup>4</sup> have been widely studied and have shown considerable technological value in many applications, for example, as electrode materials in lithium ion batteries (LIBs).<sup>5,6</sup> Where improved electrochemical performance is observed over that seen for samples containing micrometer-sized particles, this is normally ascribed to physical properties arising from the nanoscopic structure, the most obvious being the increased surface area, which results in a larger interface for  $\text{Li}^+$  incorporation, and a shorter path length for electronic/ionic transport.<sup>6,7</sup> Nanoparticles are better able to accommodate a larger amount of strain on lithiation, and this, for example, has been proposed to explain the improved performance of nanosized anatase  $\text{TiO}_2$  over micrometer-sized  $\text{TiO}_2$ . The morphological characteristics, that is, geometric shape and dimension, and the arrangement of atoms, which both vary depending on specific nanostructures, also have a considerable impact on properties such as electronic structure,<sup>9</sup> ionic diffusion, and surface structure. Determining the nanomaterials' morphology is therefore a prerequisite to a fundamental understanding of their physical and chemical properties. This Article focuses on the structural and morphological characterization of  $\text{TiO}_2$  (B) nanoparticles synthesized by hydrothermal methods, these nanoparticles receiving considerable interest,

having some of the highest electrochemical performances as LIB anode materials over all  $\text{TiO}_2$  polymorphs and morphologies prepared to date.<sup>10</sup>

Transmission electron microscopy (TEM) is routinely used to evaluate the morphology of materials on a nanoscopic scale, by examining a statistically relevant and representative number of individual particles. More comprehensive results can sometimes be achieved by incorporating a high-resolution tomographic approach.<sup>11</sup> However, if the particles are agglomerated, it becomes difficult to obtain clear and resolved images of selected single particles, and it is not always clear whether the particles that can be resolved are relevant representatives of the average morphology. In addition, structural instability of the nanoparticles has been observed under the electron beam.<sup>12–14</sup> In many cases, other techniques to assist in the microscopic analysis are essential to achieve a reliable morphology evaluation.

Scattering experiments are generally performed on an ensemble of particles, which, to some extent, compensates for the weak scattering from individual particles, and can therefore be used for nanostructure determination. Conventional crystallographic methods use Bragg scattering, which in principle correlates the scattering event with the crystal structure by a mathematical function, the Fourier transform

Received: August 10, 2015

(FT).<sup>15</sup> For crystals with very small sizes, the integration limits of their Fourier integral are considerably reduced from that of an infinite lattice to their finite dimensions in real space, thereby causing increased diffraction-peak widths in reciprocal space.<sup>16</sup> The possible coexistence of strain and a size distribution of nanoparticles will further increase the broadening effect.

Theoretically, quantitative information including the asymmetry, size, and structure of the nanoparticles can be evaluated from the position, anisotropic broadening, and relative intensity of the Bragg reflections. However, due to the peak overlap caused by peak broadening effect, some apparently resolved peaks may actually be made up of multiple Bragg reflections, and the maxima of the resolved peaks do not always align with the expected bulk peak positions.<sup>17</sup> Failure to consider all features in the diffraction pattern, and in Rietveld refinement of the structural model, can cause a misinterpretation of the data. To make full use of the diffraction data, a method utilizing the Debye equation has been applied to study the finite-size particles.<sup>17–20</sup> The computation of the scattering intensity is given by the summation of the contributions from each atom pair in the particle, and does not require long-range translational symmetry within the structure. Recently, this Debye method, coupled with Monte Carlo optimization, was used to investigate the shape of the TiO<sub>2</sub> (B) nanoparticles, and they were found to adopt prolate shapes with the *c*-axis (of the TiO<sub>2</sub> (B) unit cell<sup>21</sup>) being the major axis.<sup>22</sup>

An alternative to the reciprocal-space Bragg diffraction method is to perform pair distribution function (PDF) analysis, which is a real-space method that utilizes the total scattering, that is, both Bragg and diffuse scattering.<sup>23</sup> Because structural information is obtained on an atomic scale, the PDF method has recently proven to be an excellent tool for the study of short-range ordering occurring in nanostructured or disordered electrode materials in LIBs.<sup>24,25</sup> It has been a common practice in the structural refinement of nanoparticles,<sup>26</sup> to assume spherical particle shapes. This introduces errors when the actual shape deviates from ideal spherical symmetry, because the medium-range structural information encoded in PDF is highly correlated with the size and shape of a nanoparticle. This problem, however, can be addressed by implementing a shape function  $\gamma_0(r)$  in the PDF analysis.<sup>27,28</sup>  $\gamma_0(r)$  provides a morphological description of the actual nanoparticles and can be indirectly determined by fitting an a priori shape model to small-angle X-ray scattering (SAXS) data obtained in a separate experiment. Hence, SAXS and PDF are two complementary methods to determine morphological structural features of nanoparticles.<sup>29</sup>

In this Article, we present a comprehensive method combining both small- and wide-angle X-ray scattering techniques to study the morphology and the structure of nanoparticles, that is, shape, size, and atomic arrangement, over multiple length scales via SAXS, XRPD, and PDF analyses. Nanoparticulate TiO<sub>2</sub> (B) is chosen as our model nanostructure because it has been synthesized in the form of agglomerates.<sup>10</sup> The geometric parameters, including the shape and dimension of the TiO<sub>2</sub> (B) nanoparticles, were first obtained from the SAXS data fitting and initial PDF refinements. Using these values, various structures, including the prolate ellipsoid shape obtained from the Debye refinement,<sup>22</sup> were modeled. PDF patterns incorporating different shape functions were simulated using the various models, and the XRPD patterns for the same models were computed using

the Debye equation. Through careful comparison between the experimental data and the simulations of the PDF and XRPD pattern, we demonstrate that the TiO<sub>2</sub> (B) nanoparticles can be modeled as an oblate ellipsoid with the minor axis along the *b*-axis, and we discuss this in the context of prior results.<sup>22</sup> Identifying the morphology of this material helps to correlate the structural characteristics with its excellent rate performance; it also provides an important structural foundation for the investigation of lithiation-induced distortions on cycling TiO<sub>2</sub> (B) nanoparticles. A strain-driven distortion upon lithiation was identified and modeled for this material.

## EXPERIMENTAL SECTION

**Materials Preparation.** The TiO<sub>2</sub> (B) nanoparticles were prepared via hydrothermal methods as reported previously.<sup>10</sup> The full synthesis details and the preparation of fully lithiated TiO<sub>2</sub> (B) (referred to here as Li-TiO<sub>2</sub> (B)) are provided in the *Supporting Information*.

**Small-Angle X-ray Scattering.** SAXS data were recorded on the pristine TiO<sub>2</sub> (B) nanoparticles sealed in quartz capillary ( $\varnothing$  1.5 mm), the sample having been loaded into the capillary under an Ar atmosphere. Measurements were performed at beamline 12-BM at the Advanced Photon Source (APS) at Argonne National Laboratory, operating at an X-ray energy of 12 keV ( $\lambda = 1.033 \text{ \AA}$ ) using a MarCCD165 detector. The measured *Q*-range was  $0.014\text{--}0.4 \text{ \AA}^{-1}$ . SAXS data were analyzed using the Modeling II tool of the Irena package<sup>30</sup> within IGOR Pro. A Schulz-Zimm distribution<sup>31</sup> of particles using spheroid models with an interference structure factor<sup>32</sup> was applied.

**X-ray Pair Distribution Function via X-ray Total Scattering.** X-ray PDF via the total scattering data was collected on both pristine and fully lithiated TiO<sub>2</sub> (B) nanoparticles at beamline 11-ID-B at the APS at Argonne National Laboratory using an amorphous Si 2D detector with an X-ray energy of 58 keV ( $\lambda = 0.2127 \text{ \AA}$ ). The experiments were conducted in transmission geometry on powdered samples that were sealed in a Kapton capillary ( $\varnothing$  1.0 mm) under Ar atmosphere. The measurements, including a CeO<sub>2</sub> sample and Super P carbon as references, and an empty Kapton capillary for data background, were also performed under the same experimental conditions. Intensity data versus *Q* were obtained by converting the integrated two-dimensional (2D) image-plate data using the Fit2D software.<sup>33</sup> Data corrections including background subtraction, sample self-absorption, multiple scattering, X-ray polarization, and Compton scattering were employed to obtain the normalized scattering intensity *S(Q)* using the PDFgetX2 program.<sup>34</sup> Specifically, a *Q*<sub>max</sub> of  $25.0 \text{ \AA}^{-1}$  was used for the PDF extraction. Real-space least-squares refinement was performed using the PDFgui<sup>35</sup> program. Previously collected scattering data for the Ni standard were processed and refined to obtain the instrumental damping factor.

**X-ray Powder Diffraction.** The XRPD pattern for the pristine TiO<sub>2</sub> (B) nanoparticles was collected using a laboratory wide-angle XRPD diffractometer (Stoe STADI P) operated in transmission mode with Fe K $\alpha_1$  radiation ( $\lambda = 1.936 \text{ \AA}$ ). The XRPD pattern for the Li-TiO<sub>2</sub> (B) nanoparticles was extracted from the X-ray total scattering data with background from Super P carbon subtracted. Both acquired XRPD patterns were converted to Cu K $\alpha_1$  radiation ( $\lambda = 1.541 \text{ \AA}$ ) to allow easier comparison with the literature.

## STRUCTURE MODELING AND DATA SIMULATION

**Shape Evaluation.** TEM was previously performed on TiO<sub>2</sub> (B) nanoparticles synthesized by using an analogous method to that used by Ren et al.<sup>10</sup> The image (Figure S1) shows a severe aggregation of particles, and it is, therefore, extremely challenging to differentiate individual particles among these agglomerates. The reported morphology evaluation on a sample size of about 100 particles indicated an average size of ca.  $2.5 \times 4.3 \text{ nm}$  (width  $\times$  height) with an aspect ratio (AR =

height/width) of 1.7. As illustrated by the white rectangular boxes in the image (Figure S1), the 2D projections of these particles have elongated shapes, and hence Andreev et al. later described these particles as ellipsoids.<sup>22</sup> In the edge region of the agglomerates, where the particles are better resolved, it is clear that the projections of these particles (along one direction) are circular (highlighted with red ellipses) rather than an elongated ellipsoid (i.e., prolate). This observation likely arises from the different direction along which the particles are viewed; it, however, may also suggest that the particles may not all be prolate in shape. We have, therefore, investigated the shape of the nanoparticles using three spheroid models, including spheres, and prolate and oblate ellipsoids ( $AR_{\text{prolate}} > 1$ ;  $AR_{\text{oblate}} < 1$ , where AR is the ratio between the polar radius ( $r_{\text{major}}$  for prolate and  $r_{\text{minor}}$  for oblate spheroid) and equatorial radius ( $r_{\text{minor}}$  for prolate and  $r_{\text{major}}$  for oblate spheroid) of the spheroid (Figure 1a)).

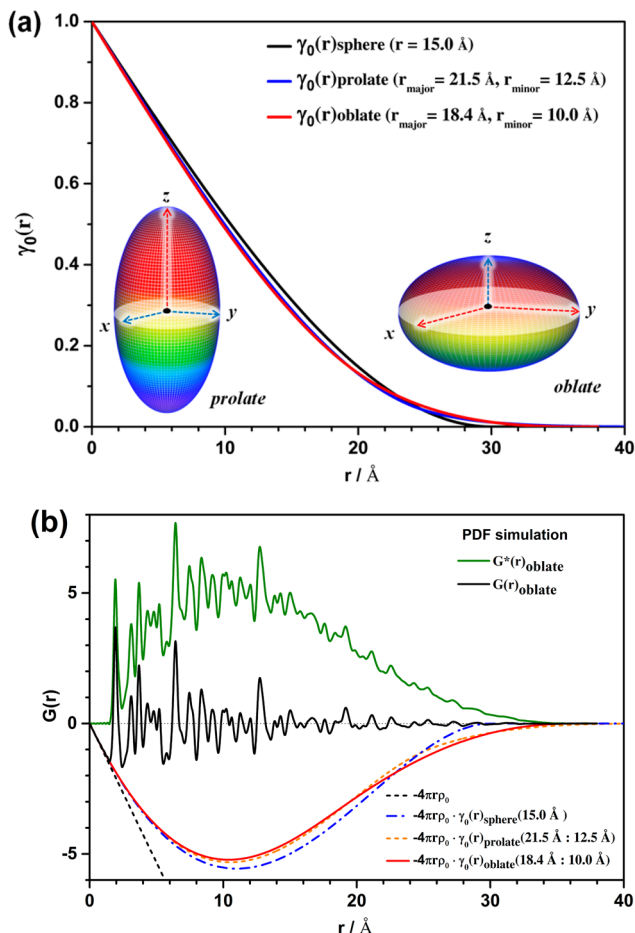


**Figure 1.** (a) Plot of the shape functions for the sphere (black), prolate (blue), and oblate (red) ellipsoids. All three particles have the same volume. The corresponding geometric parameters are labeled in the legend. An illustration of a prolate (left) and an oblate (right) ellipsoid, with  $r_{\text{major}}$  (red dashed) and  $r_{\text{minor}}$  (blue dashed) marked, is shown for comparison. (b) Examples of the  $G^*(r)$  (green solid) and  $G(r)$  (black solid) for oblate-shape  $\text{TiO}_2$  (B) nanoparticles are plotted to demonstrate the effect of the baseline correction function. These functions, incorporating the corresponding shape functions shown in (a), are plotted below the  $y = 0$  dotted line (sphere, blue dash-dotted; prolate, orange dashed; and oblate, red solid). The function for an infinitively large crystal is plotted with a black dashed line.

Three models were used to fit to the intensities of the SAXS pattern, SAXS being dependent on the size and shape (AR) of the nanoparticles. The SAXS analysis used here assumes that only the sizes of the nanoparticles vary and follow a parametric distribution, the shapes being the same for all particles (i.e., either spherical, oblate, or prolate). The accuracy of the shape evaluation relies on a precise determination of the size distribution.<sup>36</sup> Because the size distribution is not known, it is inadequate to determine the geometric shape of the  $\text{TiO}_2$  (B) nanoparticles solely from the fitting of SAXS data. Therefore, the obtained size-dependent AR derived from the respective shape model was examined and verified by complementary PDF and XRD analyses.

**Modeling of Nanoparticle Structures.** Upon obtaining the AR and size, the three spheroid structure models were constructed. The unit cell sizes and atomic positions for both the pristine and the fully lithiated  $\text{TiO}_2$  (B) nanoparticles were obtained from the structure refinement against the respective PDF data using the reported unit cell from the bulk phase<sup>37</sup> as a starting structure (Table 1). Because the occupancies of the different sites within the structure of  $\text{Li-TiO}_2$  (B) have still not been established definitively, the starting structure for the PDF refinement of the fully lithiated sample used the Li atom positions determined by computational studies.<sup>38,39</sup> Full occupancy of these sites was assumed, leading to a Li content of 1.25 per formula unit, larger than the value of 0.96 Li determined from electrochemistry (see Figure S2 for electrochemistry). Given that the scattering power of Li is very low in the X-ray experiment, the errors in the obtained structure arising from the Li occupancy, in principle, should be small. The sensitivity of the XRD method to Li occupancy did not allow for any further refinement of site occupancies. We have, however, fixed the Li positions in the refinement to avoid any unreasonable Li coordinates being produced. The PDF refinements for both the pristine and the fully lithiated samples were performed in the  $r$ -range of 1.55–15.8 Å. A short  $r$ -range was chosen because it is relatively insensitive to the particle shapes (see later discussion), and provides a reliable description of the average local structure in the absence of a model that describes the shape correctly. (This assumption will be explored later.) 1.55 Å was selected for the lower limit as  $r$ -distances less than 1.55 Å contain only termination ripples due to the  $Q_{\text{max}}$  limitation of the FT;<sup>40</sup> the upper limit of 15.8 Å, determined by the diagonal length across the unit cell body, corresponds to the longest length of a single unit cell.<sup>37</sup> To build the three models, a large three-dimensional (3D) rectangular “box” composed of stacks of repeated unit cells was first created. The origin was then translated to the center of the 3D box. The spherical model was generated by removing all of the atoms that have larger distances than “ $r$ ” from the origin, where  $r$  is the radius of the sphere. The method to construct the prolate and oblate ellipsoids is described in the Supporting Information. This structure modeling and the following data simulation were both performed using the DISCUS program.<sup>41</sup>

**Data Simulation.** The XRPD pattern for each as-constructed nanostructure was calculated via the Debye equation<sup>42</sup> (see the Supporting Information). For the pair distribution function  $G(r)$ , the geometry of the experimental data collection in practice reduces the accessible  $Q$ -range from an infinite  $Q$ -range of  $(0, \infty)$  to  $(Q_{\text{min}}, Q_{\text{max}})$ , giving rise to an experimental  $G(r)$  that differs from the theoretical  $G(r)$  denoted here as  $G^*(r)$ .<sup>27</sup> Thus, in the PDF simulation (see the Supporting Information for more details), the difference

**Table 1.** Structural Parameters for the Bulk and Nanoparticulate  $\text{TiO}_2$  (B)

parameters	literature <sup>37</sup> (bulk)	refinement (pristine nanoparticles)	refinement (fully lithiated nanoparticles)
$a/\text{\AA}$	12.1787	12.18	12.29
$b/\text{\AA}$	3.7412	3.75	3.97
$c/\text{\AA}$	6.5249	6.48	6.62
$\alpha; \beta; \gamma/\text{deg}$	90.0; 107.054; 90.0	90.00; 106.94; 90.00	90.00; 108.31; 90.00
$V/\text{\AA}^3$	284.22	283	307
$\rho/\text{g cm}^{-3}$	3.733	3.75	3.84

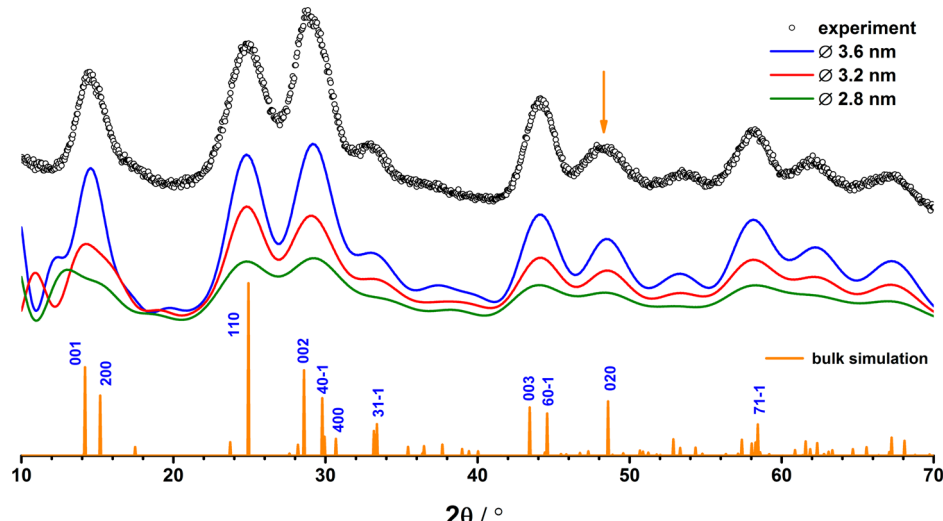


**Figure 2.** Laboratory XRPD ( $\circ$ ) as compared to the simulated pattern for bulk (micrometer-sized)  $\text{TiO}_2$  (B) (orange) and the simulations using spherical particles with diameters of 3.6 (blue), 3.2 (red), and 2.8 (green) nm. The main reflections are indexed in blue. The peak corresponding to the 020 reflection is marked with an orange arrow. The intensity reduction of the simulated pattern from the 3.6 to the 2.8 nm model is a reflection of the fewer atoms in the structure, due to the smaller size of the particle.

**Table 2.** Parameters Obtained from SAXS Fitting

parameters	sphere	prolate ellipsoid	oblate ellipsoid
aspect ratio	1.0	1.9	0.7
Schulz-Zimm mean/ $\text{\AA}$	17.3	27.9 ( $r_{\text{major}}$ )/14.9 ( $r_{\text{minor}}$ )	20.2 ( $r_{\text{major}}$ )/13.8 ( $r_{\text{minor}}$ )
Schulz-Zimm width/ $\text{\AA}$	16.4	12.4	18.2

between  $G(r)$  and  $G^*(r)$  is addressed by applying a baseline correction function, which incorporates a shape function:<sup>28,43</sup>

$$G(r) = G^*(r) - 4\pi r\rho_0\gamma_0(r)$$

where  $\rho_0$  is the average number density and  $\gamma_0(r)$  is the shape function whose physical interpretation is the probability of finding a pair of points both in the particle with a distance  $r$  in any arbitrary direction.<sup>44</sup> Given the diverse morphologies of nanomaterials, it has been common practice to assume spherical particles for PDF refinement and computation of nanomaterials.<sup>26</sup> A few studies have recently evaluated the impact of  $\gamma_0(r)$  on the resulting  $G(r)$  due to the shape deviation of nanoparticles from spherical symmetry, and a few shape functions for simple geometric shapes have been derived.<sup>45–48</sup> Among these simple models,  $\gamma_0(r)$  functions for spheroids (see the Supporting Information) are plotted in Figure 1a. Of particular relevance to this Article, the differences between the three different models, particularly between the prolate and oblate ellipsoids, are very small. Their corresponding baseline correction functions are illustrated in Figure 1b, for the  $\text{TiO}_2$  (B) structure where noticeable differences in their profiles can, however, be observed at intermediate and long ranges ( $r > 10 \text{ \AA}$ ).

## RESULTS AND DISCUSSION

**Pristine  $\text{TiO}_2$  (B) Nanoparticles.** *A. X-ray Powder Diffraction.* The calculated  $\text{TiO}_2$  (B) XRPD pattern shows multiple reflections (Figure 2) due to the low space-group symmetry of the bronze phase ( $C2/m$ ). This is the pattern that would be observed from large, micrometer-sized crystals. In comparison, the experimental XRPD shows a significant broadening, unsurprisingly leading to an extensive peak overlap, most broad peaks being composed of multiple overlapping reflections. By contrast, the peak at about  $48^\circ 2\theta$  arises almost completely from the 020 reflection. This reflection appears to be even broader than most other peaks, suggesting that the average particle probably has a smaller dimension along the  $[0k0]$  direction, the  $b$ -axis.

*B. Small-Angle X-ray Scattering.* The experimental SAXS synchrotron data on the pristine  $\text{TiO}_2$  (B) nanoparticles were fit using the three spheroid shapes, that is, spheres, prolate, and oblate ellipsoids, and the resulting parameters from the SAXS analysis are listed in Table 2, with their corresponding fitting and the radius distributions shown in Figure S4. The first fit was attempted using a spherical particle shape ( $AR = 1$ ), with a radius with an initial value of 1.5 nm (a 3.0 nm average diameter having been reported in the earlier TEM study<sup>10</sup>).

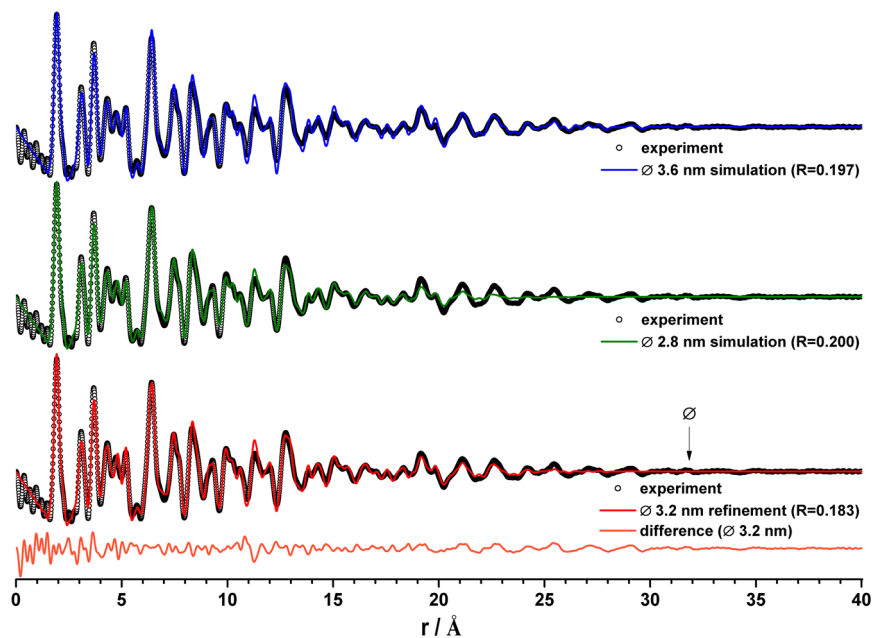


**Figure 3.** Comparison between the experimental PDF ( $\circ$ ) and the simulations using spherical models with diameters of 3.6 nm (blue) and 2.8 nm (green). The best fit was obtained in a PDF refinement using a sphere with a 3.2 nm (red) diameter (shown in the bottom, along with the corresponding difference PDF (orange)). The  $R$ -value for each model is given in the bracket. The label “ $\varnothing$ ” (diameter) marks the signal termination of the experimental PDF at about 32 Å.

This gave an optimized mean radius of 1.7 nm. The fitting using a prolate model was performed with an initial AR of 1.7 based on the reported TEM<sup>10</sup> and Debye refinement,<sup>22</sup> and it was optimized to 1.9 with a mean  $r_{\text{minor}}$  of 1.5 nm. To fit the oblate model, the initial AR was set as 0.5 (inverse of  $\text{AR}_{\text{prolate}}$ ), which was finally optimized to 0.7 with a mean  $r_{\text{major}}$  of 2.0 nm. As a result of their similar  $\gamma_0(r)$  profiles (Figure 1a) and probably large variations in size as reflected by the full width at half-maximum (fwhm, as the Schulz–Zimm width in Table 2) of each (volume-weighted) size distribution peak (Figure S4d), the three spheroid models yielded almost identical fittings (Figure S4a–c). This implies that without additional information about the particle shape, SAXS alone cannot be reliably used to distinguish between the three spheroid models. However, the three spheroid geometries (specifically, the ARs) obtained from SAXS, in combination with structural information, give rise to distinct scattering features in the wide-angle scattering data (PDF and XRPD), which can be used to investigate particle shape further, as discussed in detail in the following text.

**C. The Spherical Model. PDF.** Experimental PDF of the TiO<sub>2</sub> (B) nanoparticles in the  $r$ -range of 0–10 Å is shown in Figure S5 along with a breakdown of the contributions from different atom pairs. The first peak at 1.92 Å corresponds to the average Ti–O bond length in the first coordination shell of the Ti atoms. The second peak at 3.08 Å corresponds to the nearest Ti–Ti atom pairs. The third peak comprises both Ti–O and Ti–Ti atom pairs. The first peak has a shoulder at about 2.1 Å, which presumably arises from the elongated Ti–O bonds in the distorted TiO<sub>6</sub> octahedra. The PDF correlations become barely visible above the noise at distances greater than approximately at 32 Å (marked by “ $\varnothing$ ” in Figure 3), indicating that the average particle diameter is approximately 3.2 nm, in agreement with the reported qualitative estimates from the analysis of the TEM data.<sup>10</sup>

**Least-Squares Refinement Using PDF Data.** A real-space least-squares refinement was performed in the  $r$ -range of 0–40 Å against the structure from the reported bulk phase<sup>37</sup> (Table 1). This refinement could only be performed using a spherical model due to the current limitation of the software program.<sup>26</sup> The obtained average sphere diameter is 3.2 nm with an agreement factor  $R = 0.18$  (see the Supporting Information for definition). This refined size is consistent with the aforementioned value extracted directly from the PDF pattern, however, it is slightly smaller than the 3.4 nm value (Table 2) obtained from the SAXS fitting. In principle, the PDF measurement is weighted by mole fractions, while the SAXS fitting yields a volume-weighted size, accounting for the disagreement between two measured values. The difference between the experimental and the calculated PDF from the refinement is shown in Figure 3. A reasonably good fit is seen for the short  $r$ -range, where the residual is made up primarily of noise. However, for  $r$ -distances larger than 20 Å, the difference PDF starts to resemble a real signal, indicating that the mismatch contains actual morphological and structural information.

**PDF and XRPD Simulations.** To verify that the poor fit at  $r > 20$  Å, observed in the PDF refinement, is not simply due to the size variation of the spheres, two spherical TiO<sub>2</sub> (B) particles, one with a smaller (2.8 nm) and the other with a larger (3.6 nm) diameter, were constructed. Their corresponding PDF and XRPD patterns were simulated and compared to experiments. The PDF simulations (Figure 3) using 2.8 nm particles revealed an even larger mismatch at  $r > 20$  Å, as compared to the 3.6 nm particles. Although the 3.6 nm particle gave an excellent agreement with the experiment at longer distances, the peaks in the intermediate range from 12–20 Å showed higher intensities. These comparisons demonstrated that the mismatch between experiment and the simulated model cannot be reduced by varying the particle size within a spherical model. Particularly, the discrepancies between the

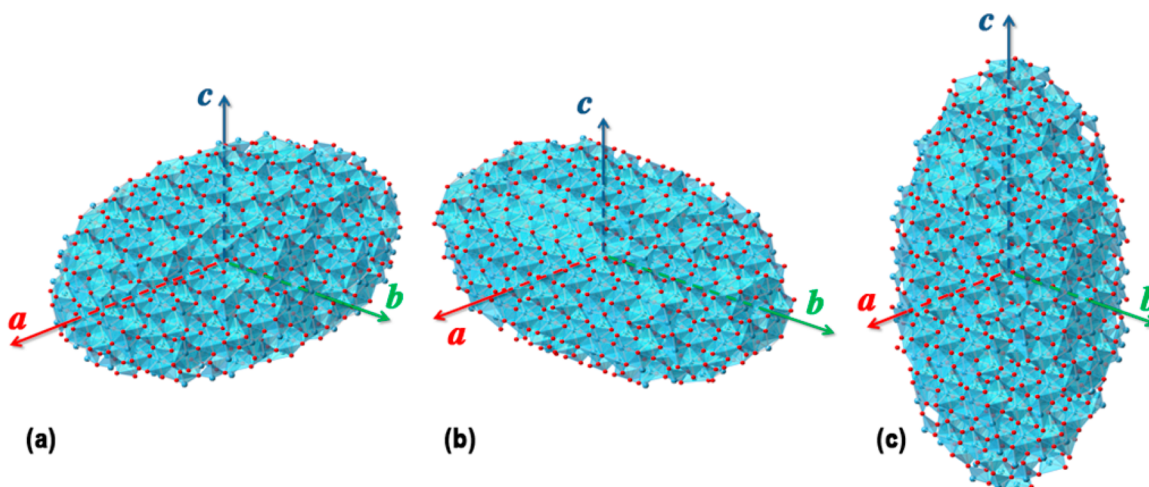


**Figure 4.** Illustrations of the prolate models ( $AR = 1.9$ ;  $r_{\text{major}} = 2.4 \text{ nm}$ ;  $r_{\text{minor}} = 1.3 \text{ nm}$ ) created from the pseudo-orthorhombic cell (Figure S3) containing Ti (blue) and O (red) atoms, with the major axis along each of the three lattice vectors: (a) prolate a, (b) prolate b, and (c) prolate c.

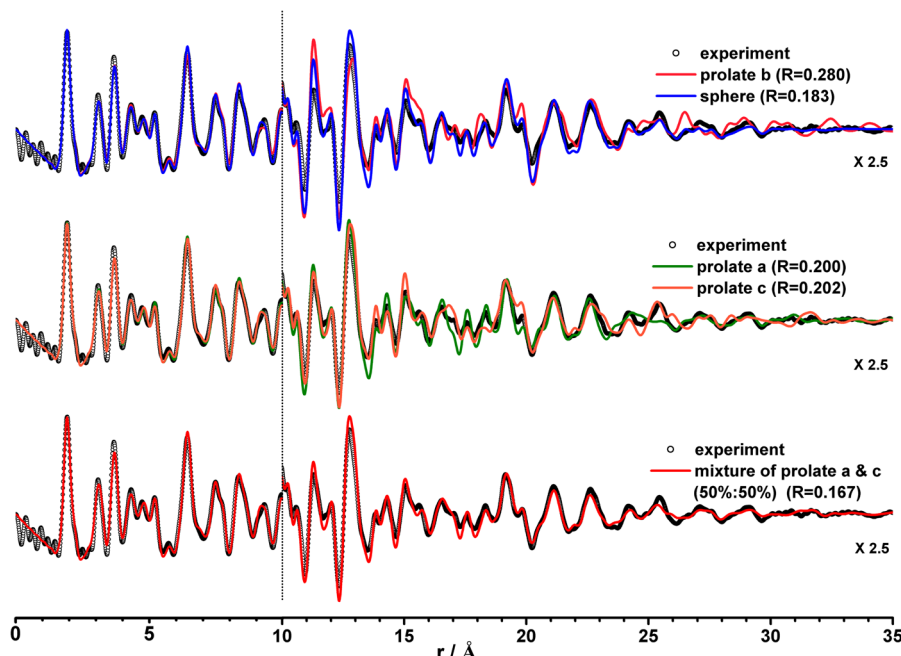


**Figure 5.** Experimental ( $\circ$ ) PDF and the simulations from the as-constructed prolate models shown in Figure 4: prolate a (green), prolate b (pink), and prolate c (orange). The refinement result indicating spherical particles with a 3.2 nm diameter (blue) and the simulation from a mixture model composed of 50% prolate a and 50% prolate c (red) are also shown for comparison. For a clearer view, the y-scales of the PDFs in the range of 10–35  $\text{\AA}$  are magnified by a factor of 2.5 relative to those shown for short ranges (0–10  $\text{\AA}$ ). The  $R$ -value for each corresponding model is given in brackets.

simulations and experiment lie in the  $r$ -range that is sensitive to particle shape (Figure 1b). This suggests that to achieve a better fit to PDF data, further attempts to include nonspherical shapes in the model are needed.

Comparisons between the experimental XRPD data and the simulations using the spherical models are shown in Figure 2. For 2.8 nm spheres, the very small size of the particles leads to considerable peak broadening that is larger than that seen experimentally, indicating that the actual particles are larger. The relative intensities of the 110 and 002 reflections depend sensitively on particle size, only the simulation with the larger 3.6 nm particles approaching the experimentally observed relative intensity. Of note, the 020 reflection ( $4.8^\circ 2\theta$ ) is noticeably broader than other resolved reflections; this

asymmetric broadening is not captured in any of the simulations using spherical particles. Again, this suggests that the average shape of the actual particles is not spherical.

**D. Prolate Model.** Three prolate models were generated with long axes along the  $a$ -,  $b$ -, and  $c$ -directions, all with ARs of 1.9 (Table 2), as determined in the SAXS experiments;  $r_{\text{major}}$  and  $r_{\text{minor}}$  were calculated by assuming that the prolate ellipsoids have the same volumes as a 3.2 nm in diameter spherical particle (the value of 3.2 nm being obtained from the PDF analysis). With the AR and volume, the geometric parameters for the prolate shape can be determined, yielding an  $r_{\text{major}}$  of 2.4 nm and  $r_{\text{minor}}$  of 1.3 nm. These values are weighted by atomic fraction, which accounts for the deviation from the volume-weighted size ( $r_{\text{minor}} = 1.7 \text{ nm}$ ) obtained from the

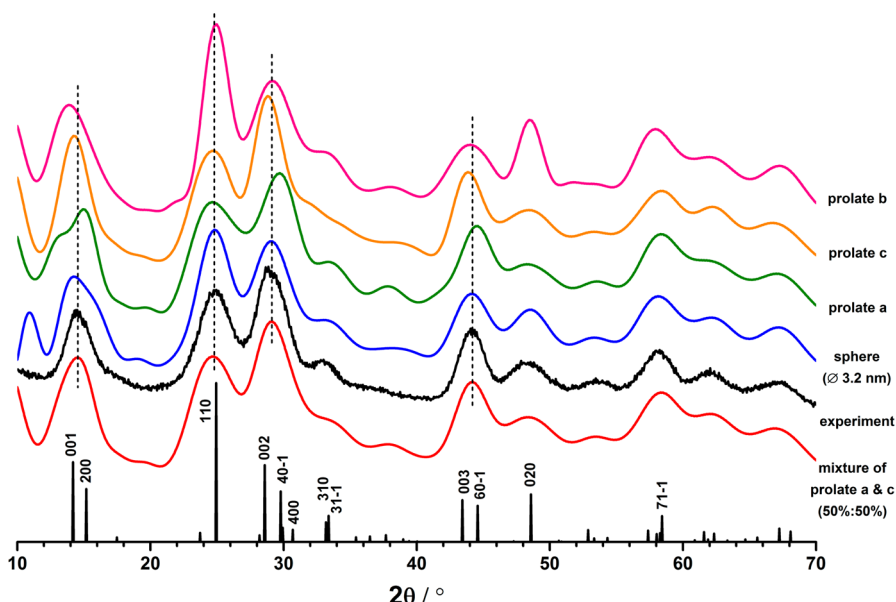


**Figure 6.** Experimental ( $\circ$ ) XRPD pattern, as compared to the simulations obtained using the same structure models used for the PDF simulations shown in Figure 5 (shown with the same color codes). An XRPD pattern simulated for a bulk (micrometer-sized) sample is shown in the bottom with the main reflection indices labeled. The dashed lines indicate the peak positions of the experimental data, to allow an easy comparison of the apparent peak shifts in the simulated patterns.

SAXS fitting. Final prolate particles (Figure 4) elongated along  $a$ -,  $b$ -, and  $c$ -axes (respectively referred to as “prolate a”, “prolate b”, and “prolate c” in further text) for PDF and XRPD simulations were built using the P1 unit cell (see Figure S3).

**PDF and XRPD Simulation.** The PDF simulations using these prolate models are shown in Figure 5, where excellent agreements with the experiment at  $r$ -distances smaller than 10 Å were observed for all three prolate models, suggesting the asymmetry of the particle makes little impact on the short-range PDF. The intensity discrepancies between the simulations and the experiment, however, become discernible at distances larger than 10 Å for all three prolate models, and vary depending on their polar axes. The poor fit using these ellipsoids, including the “prolate c” model proposed by the Debye refinement study,<sup>22</sup> is seen by comparing the  $R$ -values to that of the spherical model. The simulations of the XRPD data with these models (Figure 6, overlaid patterns are shown in the Supporting Information) are in general agreement with the PDF results. In contrast to the experiment, the broad peaks containing 001, 002, and 003 reflections, which are significantly overlapped with other reflections, show a positive and a negative (apparent) shift, respectively, for “prolate a” and “prolate c” model. These apparent shifts arise from peak overlap and reflect the relative intensities of the overlapped peaks. The simulation of the “prolate b” model yields a relatively sharp and intense peak that contains the 110 reflection, in contradiction to the experiment. Furthermore, the width of the 020 reflection in the simulation disagrees with the anisotropic broadening of the corresponding peak in the experiment, ruling out “prolate b” model as a candidate.

A more careful examination of the PDF and XRPD simulations using “prolate a” and “prolate c” model reveals that where an apparent peak shift or intensity mismatch was observed in the “prolate a” simulation, an opposite discrepancy was present in the “prolate c” simulation. Such a complementary mismatch between these ellipsoids suggests that a model that includes a mixture of the two prolate models should

be examined. Interestingly, among the mixtures with various ratios that were studied, the simulations from the 1:1 ratio showed the best resemblance to the experimental PDF and XRPD data. Taking into account that the SAXS analysis showed a similar fit to prolate and oblate shapes, and that the XRPD ruled out a prolate-b model, an oblate model contracted along the  $b$ -axis (referred to as “oblate b” hereafter) instinctively came to mind and was therefore studied.

**E. The Oblate Model.** The SAXS fitting using the oblate shape yielded a model with an AR of 0.7 and a mean major radius of 2.0 nm (Table 2). Considering the mean is volume-weighted and has a broader distribution than found for both the sphere and the prolate models (Figure S4), several “oblate b” structures with varius major and minor radii (with  $r_{\text{minor}}$  (the principal axis) oriented along the  $b$ -direction) were therefore constructed and studied, allowing us to estimate the mean value weighted by the atomic fraction. These  $r_{\text{major}}$  and  $r_{\text{minor}}$  were determined in a similar manner as the prolate model by constraining the AR at 0.7 and assuming the oblate shape has the same volume as a sphere with a radius within the range of 1.5–1.7 nm, whose mean radius (1.6 nm) was taken from the PDF refinement.

**PDF and XRPD Simulations.** Among the “oblate b” models, the one with an  $r_{\text{major}}$  of 1.9 nm and an  $r_{\text{minor}}$  of 1.3 nm (Figure 7) showed the best fits to the experiments. As indicated by the difference pattern, the disagreement with the PDF experiment (Figure 8a) was primarily evident in the  $r$ -range of 12–20 Å where the simulation showed stronger peak intensities. Such discrepancies, however, were minimal at  $r$ -distances larger than 20 Å. These observations suggest a possible loss of structure coherence at the medium  $r$ -distance due to the presence of strain within the particle. The visual comparison of the simulated and experimental XRPD data (Figure 8b) demonstrated a striking resemblance. No discernible disagreement in either peak positions or relative intensities was present, the simulated 002 reflection showing clear anisotropic broadening. A closer look at the overlaid patterns (see Figure S6) revealed

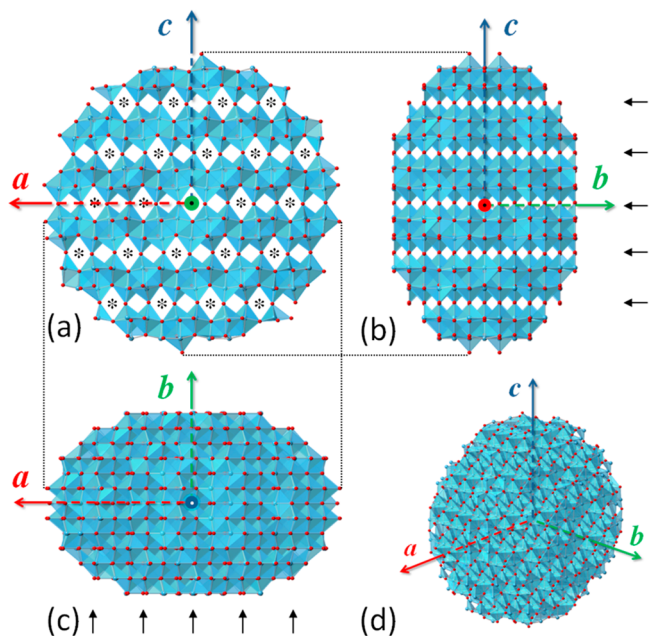


**Figure 7.** Oblate model containing Ti (blue) and O (red) atoms with an AR = 0.7,  $r_{\text{major}} = 1.9 \text{ nm}$ , and  $r_{\text{minor}} = 1.3 \text{ nm}$ , observed along (a) [010] direction, (b) [100] direction, (c) [001] direction, and (d) about [111] direction. Asterisks and black arrows indicate the diffusion channels along the *b*-axis.

an intensity mismatch for the 110 reflection at around  $25^\circ 2\theta$ . The mismatch was presumably due to the presence of a background contribution, which must in part originate from the sample holder. The presence of such a background is most evident at around  $20^\circ 2\theta$ , because in theory there are no reflections expected to be present at  $20^\circ 2\theta$ . It is difficult to model the background accurately, in the presence of broad overlapping reflections. Care must clearly be taken in interpreting the intensity of the reflections in this  $2\theta$  region,

again highlighting the point that XRPD data alone cannot provide unambiguous particle morphology information.

According to the *R*-values obtained from PDF analysis, the sphere (3.2 nm in diameter) yielded the best agreement among all of the single spheroid models apart from the mixed prolate ellipsoids (“prolate *a+c*” model). However, the spherical shape model provided a poor fit to the XRPD pattern. This implies that the *R*-values obtained from the PDF alone are relatively insensitive to the shape and the asymmetry of the nanoparticles. Also, given that neither the size distribution nor the AR was varied in the data analyses, the agreement with both PDF and XRPD experiments for the “oblate *b*” model is satisfactory. We therefore conclude that, to represent the average morphology of the  $\text{TiO}_2$  (B) nanoparticles, an oblate shape, contracted along the *b*-axis, is a better model than the prolate ellipsoid elongated along the *c*-axis as obtained by the Debye method.<sup>22</sup> The analysis also suggests that a distribution of particles cannot be excluded: a model containing a mixture of prolate particles elongated along the *a*- and the *c*-directions also gives a good fit to the experiment. Of note, the significant conclusion that emerges is that all models contain particles contracted along the [010] direction. The analysis shows that a more reliable result can be obtained by combining techniques that characterize both short- and long-range structure over that obtained when relying on only one method.

We now consider the implications of the particle morphology on the electrochemical performance, to rationalize the excellent cycling performance of the  $\text{TiO}_2$  (B) nanoparticles. Calculations<sup>38,49</sup> have indicated that the Li diffusion path in this material occurs preferentially along the channel direction, that is, *b*-axis. Among all of the structure models that have been investigated, the “oblate *b*” model maximizes the number of channels passing through the *ac*-plane (Figure 7a), increasing the active surface area for  $\text{Li}^+$  to exchange between the electrolyte and  $\text{TiO}_2$  (B) tunnels. A short *b*-dimension (Figure 7b and c) minimizes the length that the  $\text{Li}^+$  ions have to diffuse along the channel, consequently enhancing its rate capability as compared to other nanophases.<sup>10</sup>

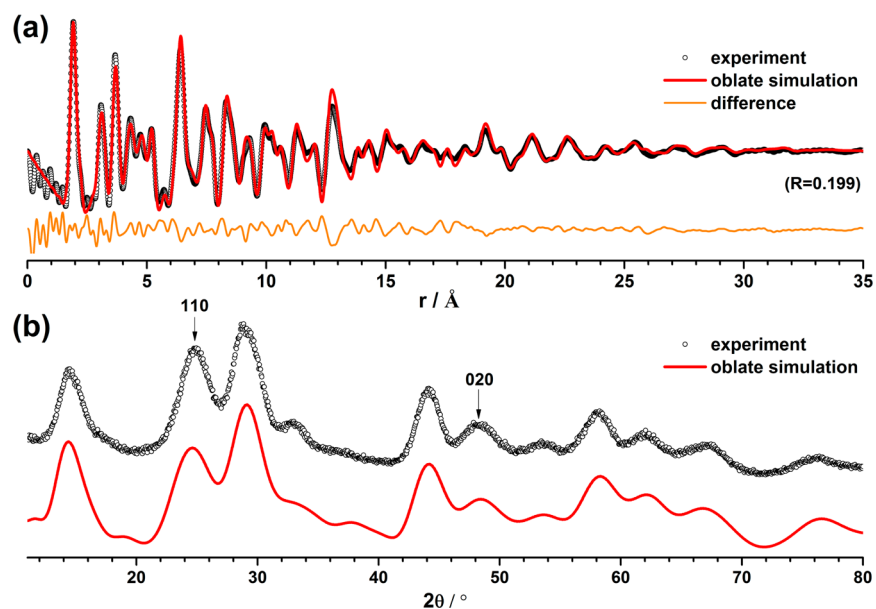


**Figure 8.** Comparison of (a) PDF and (b) XRPD data between experiments (○) and the simulations (red) using the “oblate *b*” model. The difference PDF (orange), the *R*-value from the PDF simulation, and the 110 and 020 reflections in the XRPD pattern are marked.

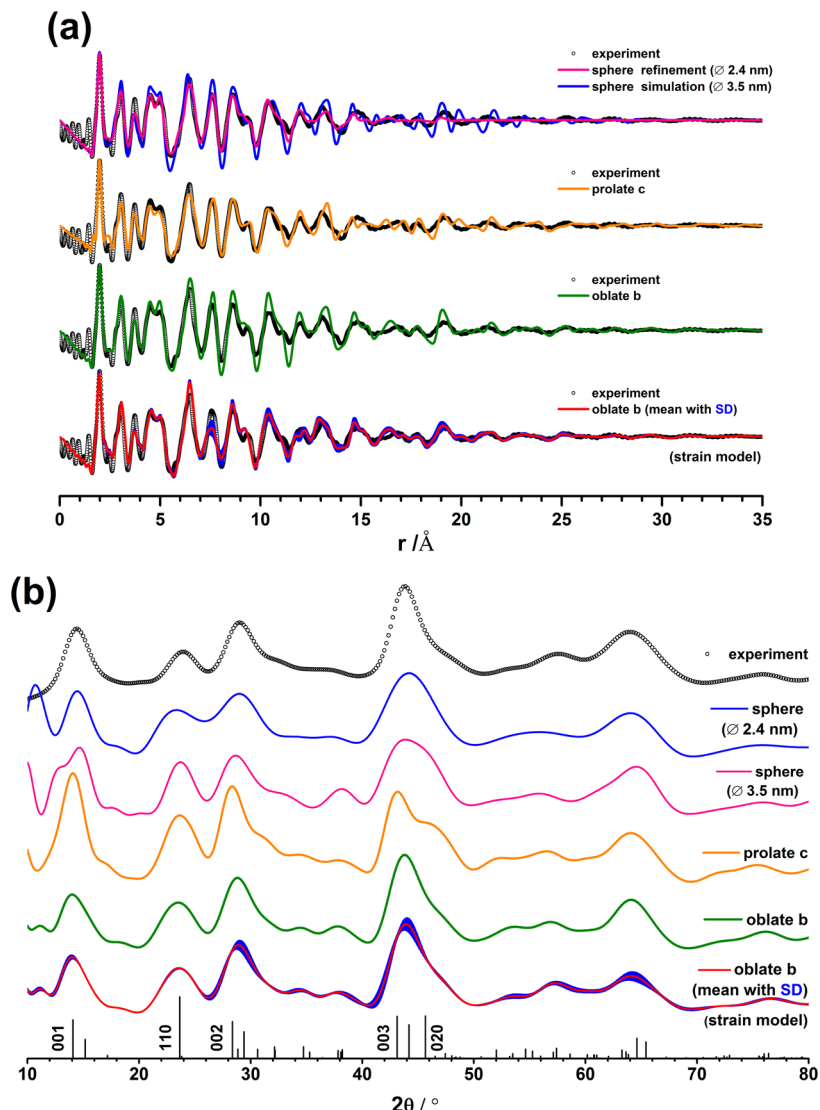


**Figure 9.** Comparison of (a) PDF and (b) XRPD data for the fully lithiated  $\text{TiO}_2$  (B) nanoparticles between experiment ( $\circ$ ) and simulations using the PDF refined spherical model (2.4 nm diameter) (blue), sphere (3.5 nm diameter) (pink), prolate c ( $r_{\text{major}} = 2.5 \text{ nm}$ ,  $r_{\text{minor}} = 1.4 \text{ nm}$ ) (orange), oblate b ( $r_{\text{major}} = 2.0 \text{ nm}$ ,  $r_{\text{minor}} = 1.4 \text{ nm}$ ) (green), and the oblate b strain model (red) averaged over 20 particles. As described in the text, the standard deviations (SD) (blue) represent the variation among the 20 particles. Bragg reflections for micrometer-sized  $\text{Li-TiO}_2$  (B) with main reflections labeled are also shown.

**Fully Lithiated  $\text{TiO}_2$  (B) Nanoparticles. A. Application of the Oblate Morphology.** To understand the electrochemical behavior of the  $\text{TiO}_2$  (B) nanoparticles further, the structure at the end of discharge was investigated. A PDF refinement of the  $\text{Li-TiO}_2$  (B) was first attempted in the  $r$ -range of 0–35 Å. The calculated PDF (Figure 9a) from the refined structure showed a mismatch in intensities for the peaks at distances larger than 15 Å as compared to the experiment. The result also indicated a particle size of 2.4 nm in diameter, even smaller than the particle size of 3.2 nm obtained from the refinement of the pristine particles, contradicting the expectation that the insertion of Li should lead to a lattice expansion resulting in a larger particle size. The corresponding XRPD simulation of this 2.4 nm sphere (Figure 9b) showed a very symmetric peak profile at around  $45^\circ 2\theta$ , inconsistent with the asymmetric peak shape observed in the experiment. These observations imply that the structure refinement of the PDF data alone is insufficient to acquire accurate morphological and structural information.

We now demonstrate the need to determine the morphology of the nanoparticles to develop a model for the structure of the  $\text{Li-TiO}_2$  (B) nanoparticles, by comparing the results obtained using the three spheroid models. The analysis started with the construction of spherical, “prolate c”, and “oblate b” particles to model the fully lithiated samples. The dimensions of the prolate and oblate geometries were calculated by multiplying their respective pristine models by an expansion factor, the lattice-constant ratio between the fully lithiated and the pristine samples (Table 1; cell parameters obtained from PDF refinements of total scattering data in the range from 1.55–15.8 Å; see methodology section). This gave rise to a prolate shape with an  $r_{\text{major}}$  of 2.5 nm and  $r_{\text{minor}}$  of 1.4 nm, and an oblate morphology with an  $r_{\text{major}}$  of 2.0 nm and  $r_{\text{minor}}$  of 1.4 nm. The size for the sphere, 3.5 nm in diameter, was calculated by assuming it has the same volume as the “oblate b” model. The PDF and XRPD simulations of these spheroid models are compared to experiment in Figure 9.

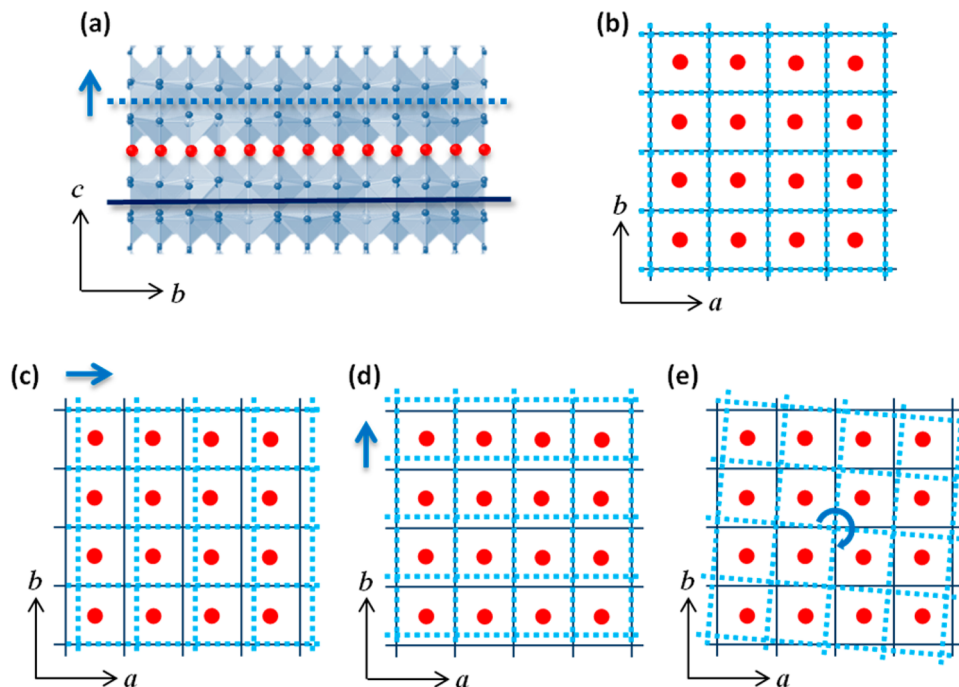


**Figure 10.** Models of strain-driven distortions in lithiated  $\text{TiO}_2$  (B). Bridging O atoms (red balls) in the  $\text{TiO}_2$  (B) structure are sandwiched by a top (denoted by a dashed light-blue line/grid) and a bottom (solid navy-blue line/grid) double- $\text{TiO}_6$  octahedral layer parallel to the  $ab$ -plane; blue arrows indicate the displacement of the top layer. (a) Displacement along the  $c$ -axis ( $c$ -shift) viewed down the  $a$ -axis. Views down the  $c$ -axis for a displacement in (b) the  $c$ -direction ( $c$ -shift), (c) the  $a$ -direction ( $a$ -shift), (d) the  $b$ -direction ( $b$ -shift), and (e) a rotation about the  $c$ -axis on the  $ab$ -plane ( $ab$ -rotation). Note that the Li atoms are omitted for a clearer view.

The PDF of the “prolate  $c$ ” model for  $\text{Li-TiO}_2$  showed a mismatch between the experimental and calculated peak positions at  $r$ -distances larger than 15 Å, as observed previously for the “prolate  $c$ ” model for the unlithiated nanoparticles. By contrast, the discrepancies between simulation and experiment for “sphere” and “oblate  $b$ ” models are primarily manifested in the peak intensities. Comparing the oblate and spherical model, the PDF simulation of the “oblate  $b$ ” particle showed a less pronounced mismatch in peak intensities than the sphere at low  $r$ -distances around 5 Å. Furthermore, a visual comparison of the XRPD simulations clearly showed that the “oblate  $b$ ” model gave the best agreement with the experiment among all of the spheroid candidates. The discrepancies in the PDF peak intensities for the oblate particle (between 5–20 Å), however, suggest a possible structure distortion that manifests itself in a loss of medium-range order. This distortion is unlikely to be a result of a random static displacement of atoms from their equilibrium positions, because this static disorder will lead to a systematic peak broadening in the PDF even at low  $r$  (see Figure S7). Hence, the loss of peak intensities in the PDF most likely stems from another effect, such as strain, this requiring more complex structure modeling for further analysis.

**B. Modeling of the Strain-Driven Distortion.** In a previous computational study<sup>39</sup> for the fully lithiated  $\text{TiO}_2$  (B) material, it was predicted that due to the occupancy of the Li sites, the distorted  $\text{TiO}_6$  octahedra in  $\text{TiO}_2$  (B) start to straighten,<sup>39</sup> potentially leading to a strain-driven distortion. Such a distortion has been previously seen for the spherical  $\text{ZnS}$  nanoparticles<sup>50</sup> as compared to bulk  $\text{ZnS}$ , giving rise to the lattice stiffening. We therefore interpret the strained structure of the fully lithiated  $\text{TiO}_2$  (B) nanoparticles in a similar manner.

As shown in Figure 10a, the bridging O atoms in the bronze phase provide a structural flexibility allowing the top double-

octahedral layer (parallel to the  $ab$ -plane) to displace from its original position relative to the bottom double-octahedral layer. Therefore, the distortion (Figure 10) can be modeled as either a slight shift of the top layer along the  $a$ -,  $b$ -, and  $c$ -directions ( $a$ -,  $b$ -, and  $c$ -shifts; Figure 10c, d, and b, respectively) or a small rotation of this layer on the  $ab$ -plane about the  $c$ -axis ( $ab$ -rotation; Figure 10e).

Simulations were obtained from an average over an ensemble of 20 particles, each containing double- $\text{TiO}_6$  octahedral layers stacked on top of each other with a random displacement magnitude over a small range (see the Supporting Information for more details). The variation between particles is reflected by the standard deviations. These displacements create medium-range structural incoherence, while the average local structure of the  $\text{TiO}_6$  octahedra remained unchanged. A preliminary evaluation of the strain effect on the scattering data due to the structural incoherence from each type of displacement was performed by visual comparison between the respective PDF and XRPD simulations from each displacement model and the experimental data (Figures S7 and S8). Although there are only marginal differences between these displacement models, a combination of  $b$ - and  $c$ -shifts, and  $ab$ -rotation was finally chosen to model the strain-driven distortion. On the basis of a visual comparison of the experimental PDF and XRPD data and the simulation for the oblate particles with and without the displacements, the simulations from the distorted model show a better agreement (Figure 9 (strain model)). Note that the improvement in the XRPD simulation is not as prominent as that in the PDF simulation, because the diffraction technique is not sensitive to structure incoherence in a short or medium range. However, an improved agreement is still evident at 50–60°  $2\theta$ .

## CONCLUSION

Conventional microscopy methods used to characterize the morphology of nanomaterials sometimes involve practical challenges arising from the aggregation of nanoscopic structure. To determine the morphology of a TiO<sub>2</sub> (B) nanoparticle sample that shows excellent electrochemical performance,<sup>10</sup> we have performed a comprehensive X-ray scattering analysis of SAXS, PDF, and XRPD data. The scattering pattern within a particular angular range encodes distinct structural features of the materials ranging from mesoscale to nanoscale. The combination of small- and wide-angle measurements therefore covers a full angular range that enables researchers to access a complete set of morphological and structural characteristics including size and shape via SAXS, particle asymmetry and long-range structure via XRPD, and short-range atomic ordering via PDF.

Pristine TiO<sub>2</sub> (B) nanoparticles with various shapes including spheres, and prolate and oblate ellipsoids were constructed on the basis of the parameters obtained from SAXS fitting and initial PDF refinement. The asymmetry of the particles was also studied. Using the resulting structural models, XRPD and PDF patterns were simulated and compared to the experimental data to develop a model that agrees with the experimental data in both short- and long-range. On this basis, we conclude that an oblate particle contracted along the *b*-axis provides a better morphology description of average TiO<sub>2</sub> (B) nanoparticles than the prolate shape elongated along the *c*-direction previously reported by the Debye study on the XRPD data. The oblate shape leads to a larger number of Li diffusion channels with shorter lengths than present in spherical or prolate particles. We believe that this contributes to the excellent cycling behavior observed for this sample, among all of the nanostructures that have been thus far reported for the TiO<sub>2</sub> (B) phase. A distribution of particle shape and size clearly exists, but of note, consistently the best model that fits all of the available data includes particles with shortened [010] axes.

To investigate the lithiation mechanism further, a structural study was also performed on the fully lithiated TiO<sub>2</sub> (B) nanoparticles. A more complex displacement model incorporating lithiation-induced strain was developed making use of the oblate particle model. It clearly shows the importance of determining the morphology of the nanoparticle so as to understand the lithiation mechanism and rationalize the rate performance of nanostructured materials. The robustness and precision of the nanomorphology and nanostructure analysis, however, lies in combining information from all three scattering techniques. Independently relying on only one of them might overlook a particular structural feature that is absent in the angular range probed by the specific technique, possibly leading to a misinterpretation of the data.

## ASSOCIATED CONTENT

### Supporting Information

The Supporting Information is available free of charge on the ACS Publications website at DOI: [10.1021/jacs.5b08434](https://doi.org/10.1021/jacs.5b08434).

Materials preparation; TEM image of the TiO<sub>2</sub> (B) nanoparticles; electrochemistry of the first discharge; modeling of ellipsoid particles; details of XRPD and PDF data simulation; shape functions for sphere, prolate, and oblate ellipsoids; R-value; fitting of the SAXS data; breakdown of atom pairs; overlaid XRPD simulations of

pristine nanoparticles using spheroid models; modeling of strain-driven distortions; and PDF and XRPD simulations of the fully lithiated nanoparticles using oblate particle incorporating strain-driven distortions ([PDF](#))

## AUTHOR INFORMATION

### Corresponding Author

\*[cpg27@cam.ac.uk](mailto:cpg27@cam.ac.uk)

### Notes

The authors declare no competing financial interest.

## ACKNOWLEDGMENTS

We acknowledge the funding from EPSRC via the “nanoionics” programme grant and a tutorial award from St. Edmunds’ College. Use of the Advanced Photon Source, an Office of Science User Facility operated for the U.S. Department of Energy (DOE) Office of Science by Argonne National Laboratory, was supported by the U.S. DOE under contract no. DE-AC02-06CH11357. We thank Dr. Sungsik Lee and Dr. Celine Merlet for their help with the SAXS experiment and structure modeling, respectively. We are grateful to Prof. Martin Dove for his time and insightful discussions and to Prof. Reinhard Neder for organizing the DISCUS workshop and for his help in the data simulation. We also thank Prof. M. Saiful Islam for many insightful discussions.

## REFERENCES

- (1) Bi, Z.; Zhang, X.; He, W.; Min, D.; Zhang, W. *RSC Adv.* **2013**, *3*, 19744.
- (2) Landi, B. J.; Ganter, M. J.; Cress, C. D.; DiLeo, R. A.; Raffaelle, R. P. *Energy Environ. Sci.* **2009**, *2*, 638.
- (3) Jiao, F.; Shaju, K. M.; Bruce, P. G. *Angew. Chem., Int. Ed.* **2005**, *44*, 6550.
- (4) Jiang, Y.-M.; Wang, K.-X.; Zhang, H.-J.; Wang, J.-F.; Chen, J.-S. *Sci. Rep.* **2013**, *3*, 3490.
- (5) Maier, J. *Nat. Mater.* **2005**, *4*, 805.
- (6) Bruce, P. G.; Scrosati, B.; Tarascon, J.-M. *Angew. Chem., Int. Ed.* **2008**, *47*, 2930.
- (7) Arico, A. S.; Bruce, P.; Scrosati, B.; Tarascon, J.-M.; van Schalkwijk, W. *Nat. Mater.* **2005**, *4*, 366.
- (8) Wagemaker, M.; Borghols, W. J. H.; Mulder, F. M. *J. Am. Chem. Soc.* **2007**, *129*, 4323.
- (9) Nunzi, F.; Storchi, L.; Manca, M.; Giannuzzi, R.; Gigli, G.; De Angelis, F. *ACS Appl. Mater. Interfaces* **2014**, *6*, 2471.
- (10) Ren, Y.; Liu, Z.; Pourpoint, F.; Armstrong, A. R.; Grey, C. P.; Bruce, P. G. *Angew. Chem., Int. Ed.* **2012**, *51*, 2164.
- (11) Thomas, J. M.; Midgley, P. A.; Ducati, C.; Leary, R. K. *Prog. Nat. Sci.* **2013**, *23*, 222.
- (12) Iijima, S.; Ichihashi, T. *Phys. Rev. Lett.* **1986**, *56*, 616.
- (13) Ajayan, P. M.; Marks, L. D. *Phys. Rev. Lett.* **1989**, *63*, 279.
- (14) Smith, D. J.; Petford-Long, A. K.; Wallenberg, L. R.; Bovin, J. O. *Science* **1986**, *233*, 872.
- (15) Warren, B. E. *X-ray Diffraction*; Dover Publications: Reading, 1969.
- (16) Woolfson, M. M. *An Introduction to X-ray Crystallography*; Cambridge University Press: New York, 1996.
- (17) Hall, B. D. *J. Appl. Phys.* **2000**, *87*, 1666.
- (18) Reinhard, D.; Hall, B. D.; Ugarte, D.; Monot, R. *Phys. Rev. B: Condens. Matter Mater. Phys.* **1997**, *55*, 7868.
- (19) Gnutzmann, V.; Vogel, W. *J. Phys. Chem.* **1990**, *94*, 4991.
- (20) Andreev, Y. G.; Bruce, P. G. *J. Am. Chem. Soc.* **2008**, *130*, 9931.
- (21) Marchand, R.; Brohan, L.; Tournoux, M. *Mater. Res. Bull.* **1980**, *15*, 1129.

- (22) Andreev, Y. G.; Panchmatia, P. M.; Liu, Z.; Parker, S. C.; Islam, M. S.; Bruce, P. G. *J. Am. Chem. Soc.* **2014**, *136*, 6306.
- (23) Egami, T.; Billinge, S. J. L. *Underneath the Bragg Peaks Structural Analysis of Complex Materials*; Pergamon: Kidlington, 2012.
- (24) Pourpoint, F.; Hua, X.; Middlemiss, D. S.; Adamson, P.; Wang, D.; Bruce, P. G.; Grey, C. P. *Chem. Mater.* **2012**, *24*, 2880.
- (25) Hua, X.; Robert, R.; Du, L.-S.; Wiaderek, K. M.; Leskes, M.; Chapman, K. W.; Chupas, P. J.; Grey, C. P. *J. Phys. Chem. C* **2014**, *118*, 15169.
- (26) Page, K.; Hood, T. C.; Proffen, T.; Neder, R. B. *J. Appl. Crystallogr.* **2011**, *44*, 327.
- (27) Mullen, K.; Levin, I. *J. Appl. Crystallogr.* **2011**, *44*, 788.
- (28) Farrow, C. L.; Billinge, S. J. L. *Acta Crystallogr., Sect. A: Found. Crystallogr.* **2009**, *65*, 232.
- (29) Gagin, A.; Allen, A. J.; Levin, I. *J. Appl. Crystallogr.* **2014**, *47*, 619.
- (30) Ilavsky, J.; Jemian, P. R. *J. Appl. Crystallogr.* **2009**, *42*, 347.
- (31) McNaught, A. D.; Wilkinson, A. *IUPAC Compendium of Chemical Terminology*, 2nd ed.; Blackwell Scientific Publications: Oxford, 1997.
- (32) Beaucage, G. *J. Appl. Crystallogr.* **1995**, *28*, 717.
- (33) Hammersley, A. 1998, FIT2D V9.129 reference manual V3.1. ESRF internal report 98HA01T. ESRF.
- (34) Qiu, X.; Thompson, J. W.; Billinge, S. L. J. *J. Appl. Crystallogr.* **2004**, *37*, 678.
- (35) Farrow, C. L.; Juhas, P.; Liu, J. W.; Bryndin, D.; Božin, E. S.; Bloch, J.; Proffen, T.; Billinge, S. J. L. *J. Phys.: Condens. Matter* **2007**, *19*, 335219.
- (36) Agbabiaka, A.; Wiltfong, M.; Park, C. *J. Nanopart.* **2013**, *2013*, 11.
- (37) Feist, T. P.; Davies, P. K. *J. Solid State Chem.* **1992**, *101*, 275.
- (38) Arrouvel, C.; Parker, S. C.; Islam, M. S. *Chem. Mater.* **2009**, *21*, 4778.
- (39) Dalton, A. S.; Belak, A. A.; Van der Ven, A. *Chem. Mater.* **2012**, *24*, 1568.
- (40) Proffen, T.; Billinge, S. J. L.; Egami, T.; Louca, D. Z. *Kristallogr. - Cryst. Mater.* **2003**, *218*, 132.
- (41) Proffen, T.; Neder, R. B. *J. Appl. Crystallogr.* **1999**, *32*, 838.
- (42) Debye, P. *Ann. Phys.* **1915**, *351*, 809.
- (43) Mullen, K.; Krayzman, V.; Levin, I. *J. Appl. Crystallogr.* **2010**, *43*, 483.
- (44) Guinier, A.; Fournet, G. *Small-Angle Scattering of X-rays*; Wiley: New York, 1955.
- (45) Lei, M.; de Graff, A.; Thorpe, M.; Wells, S.; Sartbaeva, A. *Phys. Rev. B: Condens. Matter Mater. Phys.* **2009**, *80*, 024118.
- (46) Gilbert, B. *J. Appl. Crystallogr.* **2008**, *41*, 554.
- (47) Hansen, S. J. *J. Appl. Crystallogr.* **2011**, *44*, 265.
- (48) Kodama, K.; Iikubo, S.; Taguchi, T.; Shamoto, S. *Acta Crystallogr., Sect. A: Found. Crystallogr.* **2006**, *62*, 444.
- (49) Dylla, A. G.; Henkelman, G.; Stevenson, K. *J. Acc. Chem. Res.* **2013**, *46*, 1104.
- (50) Gilbert, B. *Science* **2004**, *305*, 651.